

# Seasonal and diurnal dynamics of radio noise for 8-20MHz poleward-oriented mid-latitude radars

O.I.Berngardt<sup>1</sup>, J.-P.St.Maurice<sup>2</sup>, J.M.Ruohoniemi<sup>3</sup>, A.Marchaudon<sup>4</sup>

<sup>1</sup>Institute of Solar-Terrestrial Physics, SB RAS, Irkutsk, Russia

<sup>2</sup>Department of Physics and Engineering Physics, University of Saskatchewan, Saskatoon, Canada

<sup>3</sup>Bradley Department of Electrical and Computer Engineering, Virginia Polytechnic Institute and State University, Blacksburg, VA, USA

<sup>4</sup>Research Institute in Astrophysics and Planetology (IRAP), Toulouse University, CNRS, CNES, Toulouse, France

## Key Points:

- Physics-based seasonal-daily noise level model built for pole-oriented HF radars
- Good agreement between modeled noise level and experimental observations
- Model allows estimating vertical absorption from noise measurements

arXiv:2107.11532v1 [physics.space-ph] 24 Jul 2021

## Abstract

Based on ray tracing in a smooth ionosphere described by the IRI-2016 model we have inferred the seasonal-diurnal dynamics of radio noise observed by four mid-latitude HF radars. In the calculations, noise is assumed to propagate from the radar dead zone boundary. Noise absorption along the ray path is simulated from the IRI-2016 electron density, and from the molecular nitrogen density and electron temperatures obtained from the NRLMSISE-00 model. Model results are compared with experimental radar data, and good agreement between the two is demonstrated. The model makes it possible to estimate the amount of absorption in D- and E- layers under average undisturbed conditions. This is important for the retrieval of long term variations in the electron density in the lower ionosphere. The model also makes it feasible to interpret vertical absorption in experimental data, thereby significantly expanding the capability of HF radars to monitor the lower ionosphere.

## 1 Introduction

Noise level studies have recently become an integral part of theoretical and applied research on lower ionosphere dynamics during solar flares and coronal mass ejections through the use of SuperDARN and similar high-frequency (HF) radars (Berngardt et al., 2018; Bland et al., 2018; Berngardt et al., 2019; Bland et al., 2019; Berngardt, 2020). HF noise has traditionally been considered to come from a mixture of several components - anthropogenic, cosmic, and atmospheric.

For radars with an equatorward field of view, it has been assumed that the main contribution to observed HF noise originates from tropical lightning discharges and that the signals from these discharges propagate over large distances through the ionospheric waveguide (Pederick & Cervera, 2014). Modeling based on this notion has been validated reasonably well, with noise levels predictions close to experimental observations.

In studies by (Ponomarenko et al., 2016) and (Berngardt, 2020), seasonal-diurnal variations of the noise level were measured by the mid-latitude SAS and EKB radars at a fixed frequency. In this paper we refer to radars, including SAS, as mid-latitude radars for having geographic latitudes lower than 60 degrees. The fields of view of both radars point toward the polar regions and the shapes of the seasonal-diurnal dependence as a function of local solar time are similar. As illustrated in (Fig.1A), they take the form of an oval, the contour of which is determined by the position of the solar terminator. This stated, there is no obvious reason why the HF noise observed in mid-latitude poleward pointing radars like SAS and EKB should be closely associated with lightning. In addition, the ray paths emerging from equatorial sources are so long that the noise should be absorbed almost completely.

As a result of the above considerations, (Berngardt et al., 2019) suggested that the observed noise pattern was not so much related to the source of noise in poleward pointing mid-latitude HF radars as it was related to ionospheric conditions. The authors proposed that in most cases the sources of noise should be considered to be anthropogenic and that the noise pattern is dictated by the border of the so-called 'dead zone' often observed through ionospheric ground echoes (Samson et al., 1990). The dead zone is an area around the radar that is free of hop-propagating rays in terms the geometric optics approach that can complete a path between a ground point and the radar, hence, points within the dead zone are not sources of noise for the radar ( in terms of wave optics approach, used in this paper, some weak signals can be detected even in the dead zone ). Dead zones mark the boundary of a noise region where ray paths are focused by ionospheric effects. Specifically, this means that both the trajectory of propagation of noise signal and the intensity of the noise focusing at the border of the dead zone depend on the height distribution of the electron density along the ray path, which has clear

and strong diurnal and seasonal variations. Based on that notion, a model of the noise pattern for poleward pointing radars at mid-latitudes would have to properly account for the seasonal and daily variations of the noise level through the proper use of ionospheric and atmospheric models, given that the noise and its pattern both depend on the atmospheric and ionospheric densities through absorption and ray path focusing/de-focusing, respectively.

Mathematical empirical approaches have been introduced to reproduce noise patterns of the kind shown in Fig.1A, irrespective of the physical origin of the patterns. One such approach uses the mean daily dynamics of noise level over the previous 30 days (Bland et al., 2018). Another consists of using special auto-regressive models (Berngardt, 2020). While these models have their usefulness, no physical model has apparently been built to this day to reproduce the seasonal-daily dependence of the noise pattern. One clear advantage of building such a physical model would be the ability to predict a 'quiet-day' curve, namely, a curve of the expected noise level for ordinary ionospheric conditions. Reproducing an observed quiet-day curve would make it possible to estimate the vertical absorption level, allowing for the extraction of the long-period variations associated with the D- and E-layers of the ionosphere. In turn, building a physical model of noise level would make it feasible to effectively use SuperDARN and similar radars for estimating the electron density in the lower part of the ionosphere.

With the above in mind, we have developed a physics-based numerical model of the noise at HF frequencies. We have applied the results of the model to the seasonal-diurnal dynamics of noise level at four mid-latitude radars, namely, the Canadian SAS SuperDARN radar (52.2N, 106.5W), the US BKS SuperDARN radar (37.1N, 78.0W), the French KER SuperDARN radar (Southern French Territory, 49.2S, 70.1E) and the Russian EKB ISTP SB RAS radar (56.5 N, 58.5E). Each of these radars has a field of view with an antenna beam pattern that points nearly poleward (Fig.1B-C), meaning that the influence of tropical thunderstorm centers on the noise production should be negligible. We describe our model in Section 2. In Section 3 we present its results and compare with observations while discussing the implications for the plasma densities in the lower ionosphere. Our conclusions are presented in Section 4.

## 2 Description of the physics-based noise model

Our model is based on a mechanism proposed by (Berngardt et al., 2018, 2019). It assumes that the noise level in polar-oriented radars operating in the 8-20 MHz range is determined by a focusing of noise signals from various anthropogenic sources, and that the main sources contributing to the noise are located around the boundary of the so-called 'dead zone'. Near the dead zone, the amplitude of propagating signals is amplified significantly due to spatial focusing of radiowaves by the ionosphere (Tinini et al., 1992).

Within the framework of this model, the following factors need to be considered:

1. the spatial distribution of the amplitudes of the sources of noise and the noise emission direction pattern for each source;
2. the ray path of the radio signals in an irregular ionosphere;
3. the intensity produced by the focusing of radio signals on the boundary of the dead zone;
4. the absorption of the signal over the ray path as it passes through the D- and E-regions;
5. the antenna beam pattern of the radar receiver.

In general, each of the above characteristics has its own temporal and frequency dependencies. This stated, in the following calculations, we assumed that noise sources approx-

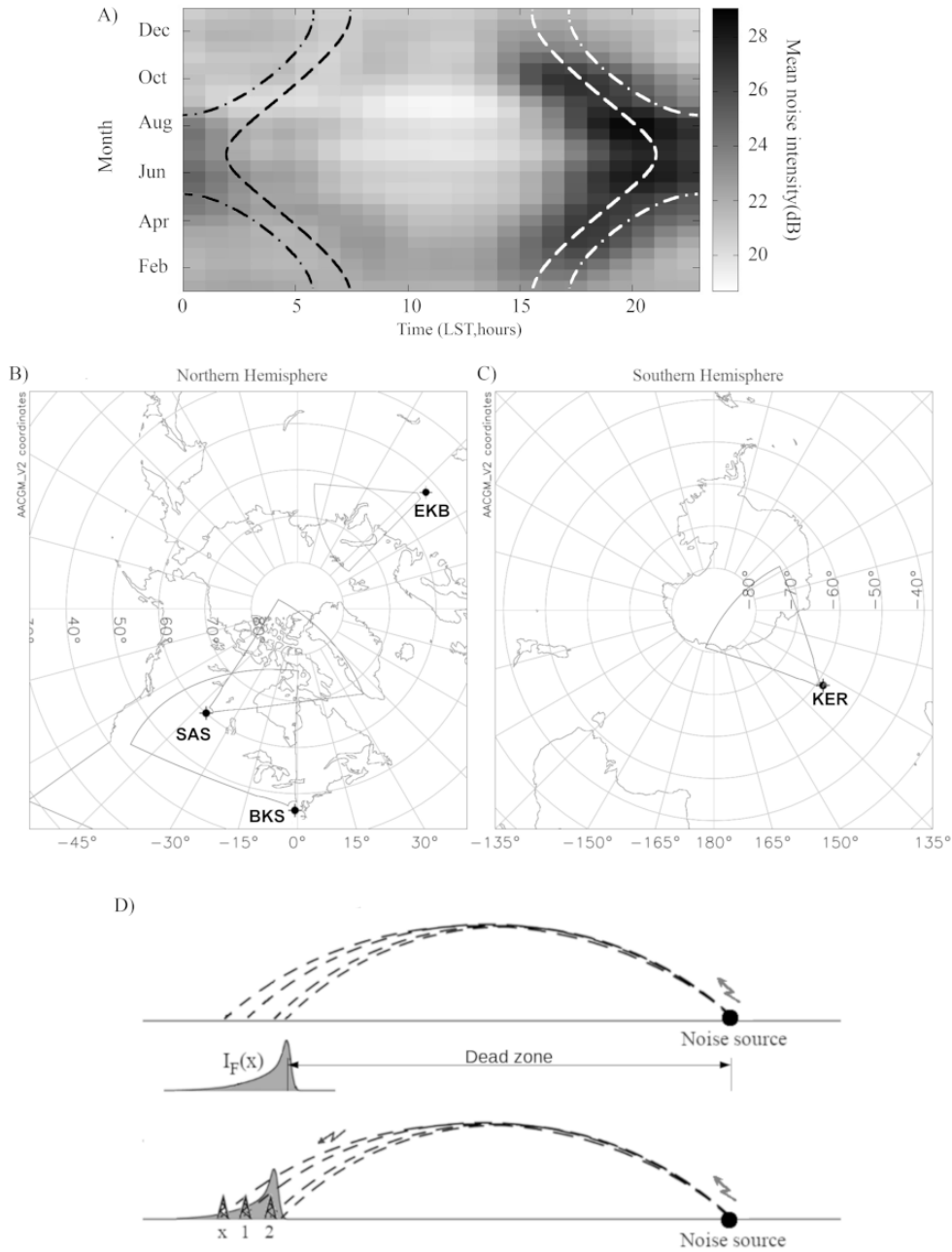


**Figure 1.** A) Seasonal-diurnal pattern of average noise intensity at the EKB radar (Bergardt, 2020). The lines correspond to the position of solar terminator at two different heights (at ground level - dashed line and at 300km height - dot-dashed line); B-C) Fields of view, in AACGMv2 (Shepherd, 2014) geomagnetic coordinates, of the four mid-latitude radars involved in the current study, for the Northern and Southern hemispheres; D) Noise propagation and collecting scheme for the proposed model, illustrating the focusing mechanism for enhancing the intensity,  $I_F(x)$ , around the boundary of the dead zone.

imately have an isotropic directional pattern, equal amplitudes, and are uniformly distributed over the Earth's surface around the radar. In the presence of intense localized anthropogenic sources (radio stations, industrial sources, railways) or for radars facing thunderstorm activity centers, this assumption has to break down. However, for radars located at a significant distance from intense anthropogenic or thunderstorm activity centers, this assumption should be acceptable.

To be specific, according to the interpretation suggested by (Berngardt et al., 2018, 2019; Berngardt, 2020) noise propagates from a noise source and focuses just beyond the boundary of the source's dead zone, as illustrated in Fig.1D. Within that framework the noise received by a radar is a superposition (integral) of noise source contributions with weights defined by dead zone multiplier  $I_F$  calculated for the radar position. The integration is made over the azimuth  $\theta$ , elevation  $\alpha$ , and range  $s$ . It takes into account the antenna beam pattern, signal attenuation with distance and signal attenuation due to absorption in the lower ionosphere. This means that, to a first approximation, the noise intensity received by the radar,  $I_{rcv}$ , can be obtained from the expression

$$I_{rcv} \approx \int_{\Omega, S} I_{src} [x(\alpha, \theta)] I_F [x(\alpha, \theta, s) - x_0(\alpha, \theta)] A_t(\alpha, \theta) G(\alpha, \theta) s^{-2} \cos(\alpha) d\alpha d\theta ds \quad (1)$$

where  $I_{src}$  is the noise intensity distribution of the noise source at the ground,  $I_F$  is the dead zone focusing multiplier,  $s$  is the distance from the source to the receiver, and  $s^{-2}$  is the attenuation in intensity due to distance. Also,  $G(\alpha, \theta)$  is the shape of the antenna beam pattern, and  $A_t(\alpha, \theta)$  is the absorption over the trajectory of a ray. In these expressions  $x$  is a phase path length along a ray that starts at specific values of  $\theta$  and  $\alpha$ , whereas  $x_0$  is the phase path length at the focusing point, namely, at the dead zone boundary. It should be understood that  $x_0$  does not depend on  $s$  but that  $x$  does depend on  $s$  because the integration is over the distances of the various noise sources to the receiver. In other words, the  $\alpha$  and  $\theta$  integrations are over the receiver angles, while the integration over  $s$  is actually over the distance of the noise sources to the radar.

As a further approximation, we assume that the variations of the various parameters are such that the noise intensity  $I_{rcv}$  can be described accurately enough with the simpler expression

$$I_{rcv} \approx I_0 \overline{I_F} A_t G_A \overline{A_R} \quad (2)$$

where  $I_0$  is the intensity of ground noise sources and replaces the  $I_{src}$  if the latter can be assumed to be isotropic (later in our simulations  $I_0$  is used as a normalization constant, calculated over one year). In addition,  $\overline{I_F}$  is the integral over all distances to the source of the focusing intensity at the boundary of the dead zone, whereas  $A_t$  becomes the absorption of the radio signal power over the whole ray path, and  $G_A$  is the beam pattern of the receiving antenna integrated over  $\theta$ , i.e., over all azimuths. Also,  $\overline{A_R}$  is the integrated signal attenuation with respect to distance. Consistent with this definition, the  $\bar{a}$  symbol describes an averaging of quantity  $a$  over the range. So to build Eq.2 we replace average value of the product of the various non-negative parameters in Eq.1 by the product of average values of the parameters with a single ray path from the border of the radar dead zone.

Finally, taking into account that power attenuates with propagation trajectory length  $s$  as  $s^{-2}$ , we can estimate:

$$\overline{A_R} \approx \int_S^{S_{max}} s^{-2} ds \approx S^{-1} \quad (3)$$

This result is valid as long as  $S \ll S_{max}$  (maximal radar range).

At a fixed frequency, we can assume  $I_0$  to be constant. This holds if we can assume to first order that the various noise sources are not only isotropic, but also homogeneous,

incoherent, and equal in intensity. This is a rather rough assumption, but, as shown below, it proves to be sufficient for an adequate modeling of the noise pattern.

## 2.1 The propagation trajectory

Propagation trajectories were obtained with the use of wave optics based on a calculation made at fixed pre-determined starting values of the elevation angles within 0-90 degrees with 0.09 degree steps. For a given azimuthal direction or radar beam we could describe the system in terms of spherical coordinates for the radial distance  $\rho$  and the elevation angle  $\phi$ . We restricted the calculations to the high-frequency limit for the index of refraction,  $n$ , and did not include absorption in the calculations, i.e., we used the ordinary wave expression given by

$$n^2 = 1 - f_e^2/f_0^2 \quad (4)$$

where  $f_e$  and  $f_0$  are the plasma frequency and radar frequency, respectively. For this situation the differential equations leading to phase and group delays as a function of starting elevation angles can be described by the following set of equations (Kravtsov & Orlov, 1983):

$$\left\{ \begin{array}{l} \frac{\partial R_\rho}{\partial s} = P_\rho \\ \frac{\partial R_\phi}{\partial s} = \frac{1}{R_\rho} P_\phi \\ \frac{\partial P_\rho}{\partial s} = \frac{f_e}{f_0^2} \frac{\partial f_e}{\partial R_\rho} + \frac{1}{R_\rho} P_\phi^2 \\ \frac{\partial P_\phi}{\partial s} = \frac{1}{R_\rho} \left( \frac{f_e}{f_0^2} \frac{\partial f_e}{\partial \phi} - P_\rho P_\phi \right) \\ \psi = \psi_0 + \int_{S_0}^S P^2 ds \end{array} \right. \quad (5)$$

where  $\vec{R}$  is the radius vector describing the position of the wave impulse at a particular point in the trajectory and where  $\vec{P}$  is the wave impulse, while  $\psi$  is the phase path (or eikonal). Integration was carried over the trajectory variable  $s$  with starting and end points at  $S_0$  and  $S$ , and with  $\psi_0$  being associated with the initial value of the eikonal. In such calculations, the regions where phase delay goes through an extremum (minimum) correspond to the regions of focusing, that is to say, they describe the borders of the dead zone for different propagation modes.

In the numerical calculations giving rise to our model, we assumed that the radio wave propagated in a plane that was associated with a given azimuth over a globe arc within the framework of the spherical Earth model. This stated, our ionospheric model remained inhomogeneous in the propagation plane, namely, over the distance to the source and the elevation angle. In other words the ionospheric model remained a function of latitude and altitude. Specifically, we used the IRI-2016 (Bilitza et al., 2017) ionospheric model for this purpose. In order to work with a smooth and continuous ionosphere along the trajectory, it was necessary to assume that the signal propagation plane did not depend on the starting elevation angle when seeking numerical solutions to the set of differential equations (5). While correct for the middle(central) beams of the radar antenna pattern, this was not strictly true for the extreme ones, since the antenna beam pattern is actually described by a conical shape (Shepherd, 2017). But, as will be shown later, this rough approximation is sufficient for carrying the model calculations forward with reasonable accuracy.

For the specific ray path calculations we used a grid with step sizes of 222 km (equivalent to  $2^\circ$  in latitude at Earth's surface) in distance and 3 km in height in the propagation plane. For calculations between grid points, an interpolation was performed using two-dimensional local quadratic B-splines to obtain continuous values and smooth

spatial derivatives. When later adding absorption effects we used the the NRLMSISE-00 model for the neutral atmosphere, from which we extracted the molecular nitrogen density and the electron temperature interpolated between grid points in the same way.

## 2.2 Modeling the focusing near the dead zone boundary

### 2.2.1 Determining $\overline{I}_F$

In a two-dimensional situation such as the one used here, the focusing of the radio waves emitted from a point source can be described analytically near the dead zone, if the ionospheric peak can be approximated by a parabola. In that case, if we neglect insignificant multipliers, the signal amplitude  $A_F(x)$  over the phase path length  $x$  has a well-known dependence given by (Tinini et al., 1992):

$$A_F(x) \sim \frac{1}{\Lambda} Ai\left(\frac{2^{2/3}}{\Lambda} [\bar{x} - x]\right) \quad (6)$$

where  $Ai()$  is the Airy function describing the shape of the signal focusing versus phase path length, and where

$$\Lambda = \left( \frac{1}{2k^2} \frac{\partial^2 \bar{x}}{\partial \alpha^2} \right)^{1/3} \quad (7)$$

is a quantity inversely proportional to the size of the focusing area associated with the second derivative of the phase path length over the elevation angle  $\alpha$ . Note that Equation (6) does not take into account the decay of the wave field with distance.

By integrating (6) over the range, and taking into account that noise sources are independent, it therefore follows that the range-integrated power  $\overline{I}_F$ , corresponding to the total power of the noise superposed from various noise sources homogeneously placed at different ranges is given, to a first approximation, by:

$$\overline{I}_F \sim \frac{1}{\Lambda} \int Ai^2(\bar{\eta} - \eta) d\eta \quad (8)$$

where the integration is made over the dimensionless quantity  $\eta = 2^{2/3}x/\Lambda$  and  $\bar{\eta} \gg 1$ .

This means that the focusing power  $\overline{I}_F$  in (2) thus can be approximated reasonably well with the simple expression:

$$\overline{I}_F \sim \frac{1}{\Lambda} \quad (9)$$

### 2.2.2 Determination of the dead-zone position

To find the propagation path of the focusing signal in an arbitrary ionosphere, it is necessary in the context of wave optics to extract the dependence of the phase delay  $\psi$  on the elevation angle  $\alpha$ . We use the fact that, at the focal points, the phase delay dependence on the elevation angle is weakest, meaning that the derivative of the phase becomes zero (Tinini et al., 1992). Since we considered many possible ray paths, the focal points spread into a small area. Qualitatively, the size of such an area is a measure of the number of rays arriving at the receiving point with the same phase, thereby adding to the total amplitude of the received noise signal through constructive interference of the rays. In terms of our model, this size is inversely proportional to the cubic root of the second derivative of the phase delay over the elevation angle (Eq.7) at the point where

the first derivative becomes zero (i.e. near the dead zone border), so that the power of the focused signal is proportional to the size of this area (Kravtsov, 1968).

It is obvious that in a complex ionosphere there can be several focusing regions (modes). To find the positions (elevation angles) of the groundscatter modes, we analyzed all the possible propagation trajectories by calculating the phase delay  $\psi$  for each elevation angle  $\alpha_i$ . After calculating the dependence of the phase delay on the elevation angle  $\psi(\alpha)$  the elevation angles  $\alpha_i$  of the rays getting to the dead zones were determined from the position where the phase delay reached its minimal value:

$$\alpha_i : \left. \frac{d\psi(\alpha)}{d\alpha} \right|_{\alpha=\alpha_i} = 0 \quad (10)$$

We should add that the local dependence  $\psi(\alpha)$  was fitted to a parabola to make the evaluation of the second derivative of  $\psi(\alpha)$  more easily to facilitate the evaluation of  $\Lambda$  (Eqn 7).

We obtained a collection of angles  $\alpha_i$  corresponding to different groundscatter modes. In a regular, spherically layered, non-magnetized, parabolic ionosphere, there is usually no more than one ground-scatter mode - there is only one local minimum of the phase-elevation characteristic. In a more complex but more realistic heterogeneous multi-layer ionosphere, there can be several groundscatter modes, with the presence of a magnetic field possibly adding extra possibilities. Just with the propagation of ordinary rays, we found many instances of multiple ground-scatter modes, each with its own phase, group delay and central elevation angle  $\alpha$ .

Examples of electron density profile at different local time(LT), as well as phase and group delay for single-mode (black line) and multi-mode (red and green lines) signals, calculated using the IRI-2016 model, are shown in Fig.2A-C. Modeling was carried out for the EKB radar (56.5N, 58.5E), for the northern direction of radio wave propagation (azimuth 0, beam 2), for June 1, 2013. It can be seen from the figure that several modes correspond to several well-defined (E and F) layers in the electron density.

When multi-mode noise trajectories were obtained, we chose the mode (trajectory) that contributed the most to the noise signal intensity, after having taken signal absorption and antenna pattern attenuation into account. Following this, the modeled noise level was chosen to be the intensity of the mode with maximum intensity after taking all factors into account, namely, propagation, absorption, and antenna beam pattern.

### 2.3 Antenna pattern

Another important parameter of the model is the signal attenuation due to the antenna pattern  $G_A$ . The attenuation can reach several tens of dB, and therefore it is very important to take it into account at low and high elevation angles. In this paper, we have dealt with the data from several radars: EKB from ISTP SB RAS, and SAS, KER and BKS from SuperDARN. Every one of these radars has a different type of antenna and a different  $G_A$ .

Taking into account that the azimuthal width of the antenna beam pattern is defined by a phased array geometry and size considerations (that much is similar for all the radars under consideration), the integrated antenna multiplier  $G_A$  has been taken to simply be proportional to the antenna pattern in the elevation plane, that is to say:

$$G_A(\alpha) = \int_{\Omega} G(\alpha, \Theta) d\Theta \approx G(\alpha) \Delta\Theta \quad (11)$$

where  $\Delta\Theta$  is the azimuthal beam width of the phased array antenna beam pattern and is the same for all the radars considered here. In addition,  $G(\alpha)$  is the antenna beam pattern of a single antenna in the elevation plane.



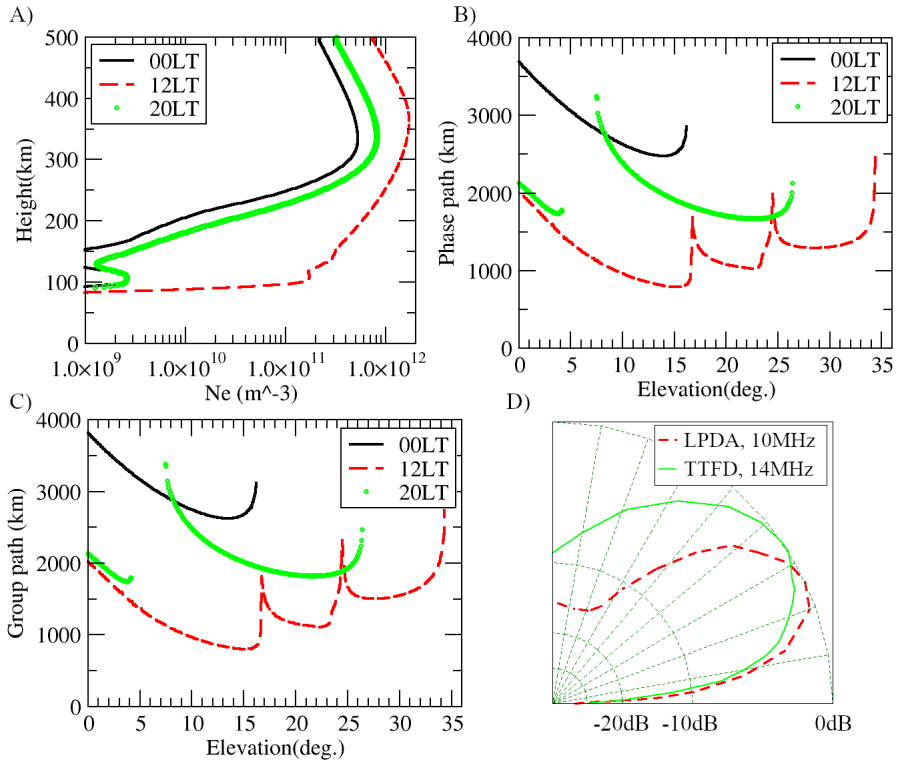


**Figure 2.** A-C)-Examples of electron density profile (A), phase path (B) and group path (C), calculated using the IRI-2016 model for the EKB radar for the north-facing direction on 01 June, 2013; D) - model radar antenna beam patterns in the elevation plane used in our various simulations: LPDA beam model at 10 MHz for the EKB, SAS and KER radars (Berggardt et al., 2020; Arnold et al., 2003), and TTFD beam model at 14 MHz for the BKS radar (Sterne et al., 2011).

Fig.2D shows the model antenna beam patterns of the various radars at 10-14 MHz frequency that were used for our modeling. It should be noted that the main difference between the various antenna beam patterns comes from the fact that the EKB, SAS and KER radars use Log-Periodic Dipole Array antennas (LPDA) at the top of masts approximately 15 meters above the ground (Arnold et al., 2003; Bergardt et al., 2020), while the BKS radar uses Twin Terminated Folded Dipole antennas (TTFD) at a lower height (Sterne et al., 2011). This significantly increases the amplitude of the vertical lobe on the BKS radar and broadens its elevation antenna pattern as compared to the EKB, SAS and KER radars.

## 2.4 Noise absorption over the trajectory

Another important parameter affecting the radio noise intensity is the absorption of the signal over the propagation trajectory. The absorption per unit length  $L[dB]$  was calculated within the framework of a classical model (Zawdie et al., 2017) in which frequencies are considered to be high enough to justify neglecting magnetic field effects:

$$L[dB] = -\frac{20}{\log(10)} \frac{e^2}{2\epsilon_0 m_e c} \frac{n_e \nu_e}{\nu_e^2 + (2\pi f_0)^2} \quad (12)$$

where, as before,  $f_0$  is the operating frequency of the radar,  $n_e$  is the electron density, and  $m_e, c, \epsilon_0$  are the electron mass, the speed of light in vacuum and the dielectric constant of vacuum, respectively while  $\nu_e$  is the effective electron collision frequency. Since  $\nu_e$  is only effectual in the lower part of the ionosphere we considered it to be equal to the electron collision frequency with molecular nitrogen  $\nu_{e,N_2}$ . Using (Schunk & Nagy, 2000), it was assumed to be given by:

$$\nu_e \simeq \nu_{e,N_2} = 2.33 \cdot 10^{-11} \cdot n_{N_2} (1 - 1.21 \cdot 10^{-4} T_e) T_e \quad (13)$$

where  $n_{N_2}$  is the molecular nitrogen density and  $T_e$  is the electron temperature. The accuracy of this approximation has been discussed in detail by (Zawdie et al., 2017).

The total absorption of the radio wave  $L_{int}[dB]$  was calculated as the integral of the unit absorption over the propagation trajectory  $S$ , namely, (Zawdie et al., 2017):

$$L_{int}[dB] = \int_S L[dB] ds \quad (14)$$

In the simulations, the absorption was taken into account only for the D- and E-layers, namely, in the 60-120 km altitude range, where significant contributions to the absorption were possible if  $n_e$  was potentially large enough and where the collision frequency could compete with  $f_0$ . For our model simulations, we describe the absorption factor  $A_t$  in Eqn (2) with

$$A_t = \exp\left(\frac{\ln(10)}{10} L_{int}[dB]\right) \quad (15)$$

### 2.4.1 Weighting the factors that control the absorption

To evaluate the absorption of the radio signal from the above expression, we used well-known empirical models, namely, the IRI-2016 model for a determination of the electron density  $n_e$ , and the NRLMSISE-00 model for a determination of the effective electron collision frequency based on the density of molecular nitrogen  $n_{N_2}$  and the electron temperature  $T_e$ . For calculations between grid points, interpolation was performed with two-dimensional local quadratic B-splines to obtain continuous values required for trajectory calculations. Then, in the plane of the propagation trajectory of the radio signal, the absorption was tabulated over a grid which had 222 km range resolution and

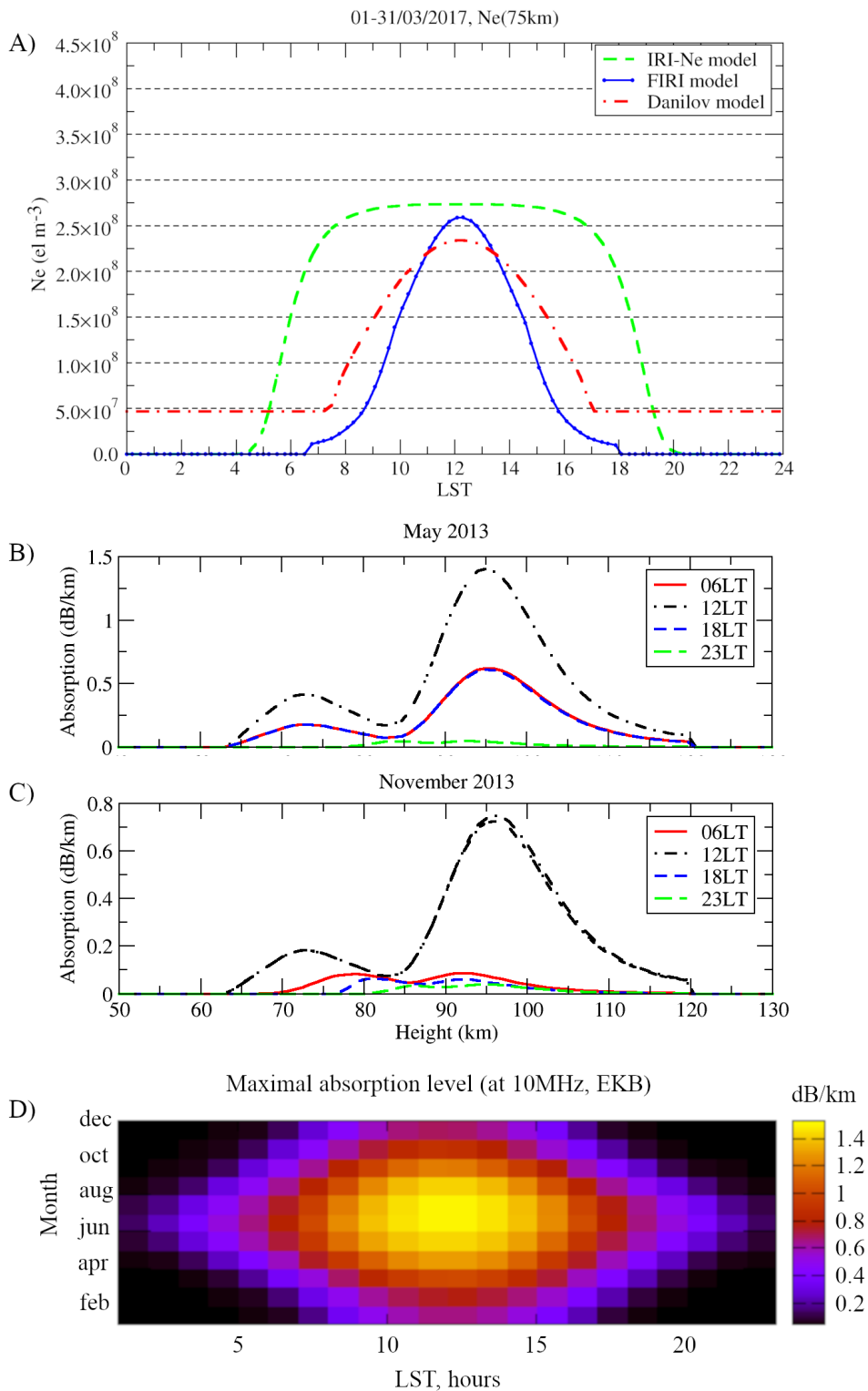


**Figure 3.** Panel A: Comparison between the monthly average and median electron densities at 75 km altitude extracted from the three different models listed in the legend. Panels B to D: Modeling results for beam 2 of the EKB radar, beam 2 ( $0^\circ$  azimuth) for the year 2013, based on the standard IRI-Ne option of the model IRI-2016. Panel B: modeled absorption profile per 1 km propagation trajectory for May 2013. Panel C: same as for panel B but for November 2013. Panel D: seasonal-daily variation of the maximum value of the absorption per 1 km of the radio signal trajectory in the ionosphere.

5 km height resolution. In the simulations, interpolation based on local quadratic B-splines was once again used to account for a smooth spatial dependence.

One source of uncertainty in the absorption calculation comes from accounting for the electron density in the D-layer, which is no easy task, to say the least (Danilov et al., 2002; Bilitza & Reinisch, 2008). Even the standard Reference ionospheric model, IRI-2016, includes several different models for electron density at heights 65-110 km. To demonstrate the complicated task at hand, Fig.3A shows a comparison of the monthly average level of electron density at 75 km height between three electron density models for the March 2017 (IRI, FIRI and Danilov's). The IRI-2016 model comes with the standard IRI-Ne D-layer model. Other models of the D-layer come from (Danilov et al., 1995; McKinnell & Friedrich, 2006).

Fig.3A shows that there are clearly important differences in the D region between the models. In particular, the nighttime electron density level could be significant (as demonstrated, for example, in (Gomonov et al., 2019)) and should be taken into account when simulating the diurnal variation of the absorption. Taking this into account leads us to conclude that the diurnal variation of the absorption inferred from the ionospheric models is associated not with the absolute value of the electron density, but with its variation over its minimum (nighttime) value. This means that the absolute electron density of the D-layer cannot be correctly determined through coherent scatter radar absorption data using noise level observations without a very careful analysis of the latter and without an absolute calibration of these observations on a long term basis. A comparison between observations and numerical prediction is done in the next subsection.

Before a detailed comparison we want to illustrate the effect of seasonal variations on absorption, Figures 3B and 3C show plots of the unit absorption per kilometer of the trajectory  $L[dB]$  as a function of altitude that were calculated for May and November of 2013 to the North of the EKB radar (azimuth 0 degrees, radar beam 2), using the standard IRI-2016 model to describe the D-layer. The radiowave propagation path used for the calculation corresponds to the trajectory of the groundscatter signal propagation, i.e. to the trajectory from the dead zone boundary to the radar. The absorption values are close, in the end, to the results obtained by (Zawdie et al., 2017).

Figure 3D also shows the full seasonal-daily variation of the maximum value  $L_{max}[dB]$  of absorption per km of the trajectory in the ionosphere

$$L_{max}[dB] = \text{Max}(-L[dB])_{h=[60..120km]} \quad (16)$$

The calculation is based on the standard IRI-2016 D-layer model for the EKB radar site. As can be seen, the maximum absorption is observed in the summer under daytime conditions. This is the result of the ionization of the lower part of the ionosphere being greatest at that time of day and year. It contrasts with winter and/or nighttime conditions when the lower ionosphere should have only weak ionization if any at all, according to the empirical models.

### 3 Results and discussion

#### 3.1 Comparison between simulations and experimental observations

For the years 2013 and 2014, we have compared the observed noise level for our four mid-latitude radars with calculations based on our noise level model using three different D-layer models included into the international reference ionospheric model IRI-2016: (1) the standard IRI-Ne (Bilitza, 1997) model, (2) the FIRI model (McKinnell & Friedrich, 2006) and (3) the Danilov model (Danilov et al., 1995). The comparisons are shown in Fig.4.

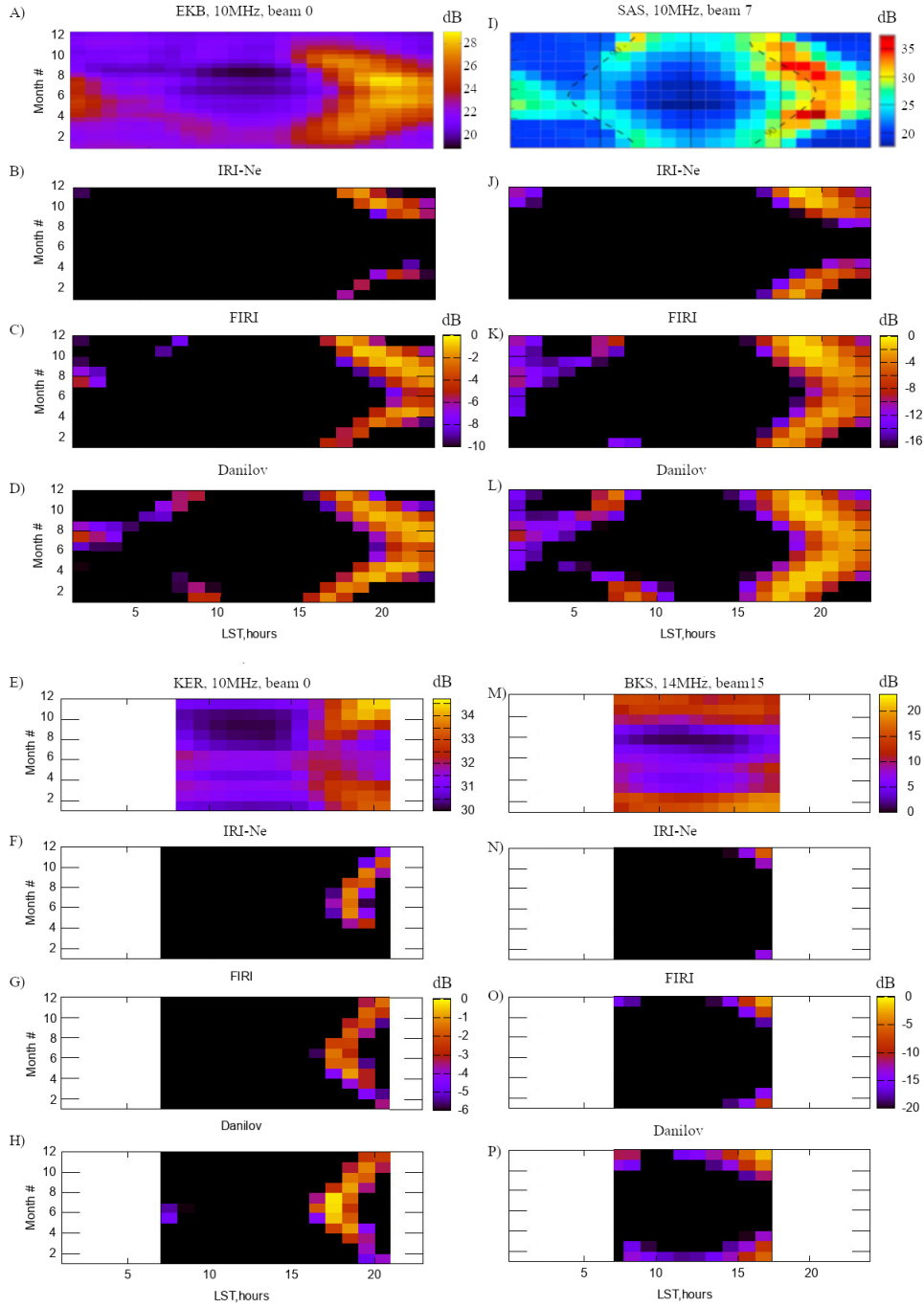


**Figure 4.** Comparison between observations and simulations of noise level seasonal-daily dependence for 2013 based on three different D-layer models, namely, IRI-2016, FIRI, and Danilov. Panels A to D: EKB radar, 10MHz, at  $0^\circ$  azimuth with the top panel for observations and the next 3 panels for each model. Panels E to H: same as panels A to D, but for the KER radar at 10 MHz for a  $180^\circ$  azimuth. Panel I: SAS observations reported by (Ponomarenko et al., 2016). Panels J to L: same as panels B to D, but for the SAS radar at 10 MHz for a  $-23^\circ$  azimuth. Panels M to P: same as panels A to D but for the BKS radar at 14 MHz at  $0^\circ$  azimuth.

A detailed comparison can be made with more confidence for the data associated with the EKB and SAS radars, because the data from these radars came from noise level observations at a fixed frequency close to 10 MHz on a 24 hours per day basis. From the results displayed in Figs.4A to 4D, and 4I to 4L for the EKB and SAS radars respectively, it can be seen that using standard IRI-Ne D-layer model leads to a significant overestimation of noise absorption, while the FIRI and Danilov models lead to better qualitative agreement between model calculations and observations in regions away from the regions of low noise prediction by the model (i.e., the uniformly dark central areas in the panels that describe the computational results).

Data from the BKS and KER radars are harder to use for a comprehensive analysis because they come from a variety of daytime and nighttime sounding conditions. Nevertheless, the daytime data that were retrieved (for 14 MHz at BKS, and for 10 MHz at KER) demonstrate a good agreement with our model, particularly for the KER radar and especially when using Danilov's model of the D-layer.

As one can see, the KER radar (southern hemisphere) seasonal-daily noise has a distribution that differs significantly from the northern hemisphere EKB, SAS and BKS radars. This difference appears to come from the difference in hemispheres that are to be associated with different seasons and atmosphere/ionosphere conditions. Indeed our model shows a good correspondence with the observations in both the northern and southern hemispheres, implying that the model that we formulated based on Eqn. (2) has validity.

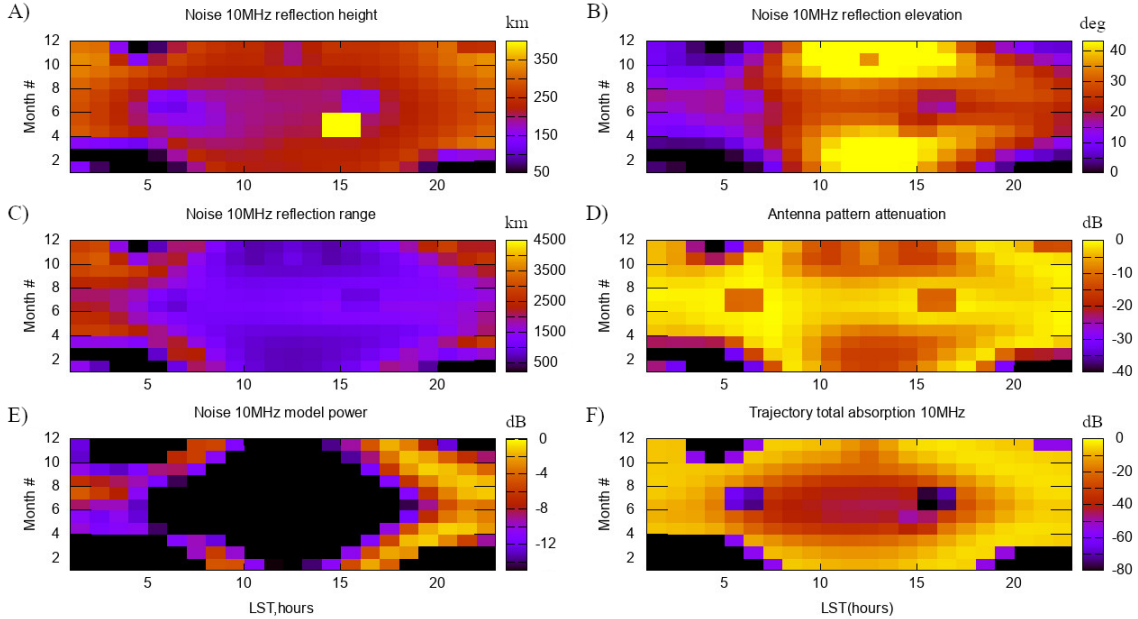
### 3.2 Relationship between propagation parameters and noise variations

For a qualitative analysis, it is useful to demonstrate the relationship between the propagation parameters and the seasonal-diurnal variation of the noise level. Fig.5 shows the simulated results of seasonal-diurnal variation of various propagation parameters at the EKB radar. It can be seen from the figure that:

- the annular shape of the noise level (Fig.5E) is controlled mainly by the total absorption over the propagation trajectory (Fig.5F): in other words, the more absorption there is, the less noise is seen, with the two patterns matching very well;
- the total absorption over the trajectory, in turn, is related to the trajectory elevation angle (which changes the propagation length of the signal in the absorbing layer) - the higher the elevation angle, the shorter this length and the higher the noise level (Fig.5B).
- the total absorption is also related to the unit absorption in the regular D- and E-layers - the stronger the absorption, the lower the noise level(Fig.5F versus 3D). We should note that preliminary modeling has shown that the absorption below 85 km altitude is comparable to the absorption above 85 km;
- the attenuation of the noise level in the winter daytime is associated with antenna pattern attenuation at high elevation angles(Fig.5D versus Fig.5B).

### 3.3 Saturation effect and quiet day curve

As could be inferred from Fig.5 the central region embedding summer daytime conditions seems to be associated with noticeably weaker noise levels than expected from the model calculations. The predictions for weak noise levels are based on strong absorption during sunlit conditions so that little noise from ground sources should be expected to be found. We have carried out more detailed comparisons to assess this situation. For the purpose at hands, we focused on only two radars (EKB and SAS) because these were radars that used a fixed sounding frequency (10 MHz) on a continuous basis throughout the day. This allows for a numerical comparison between the model and observations:



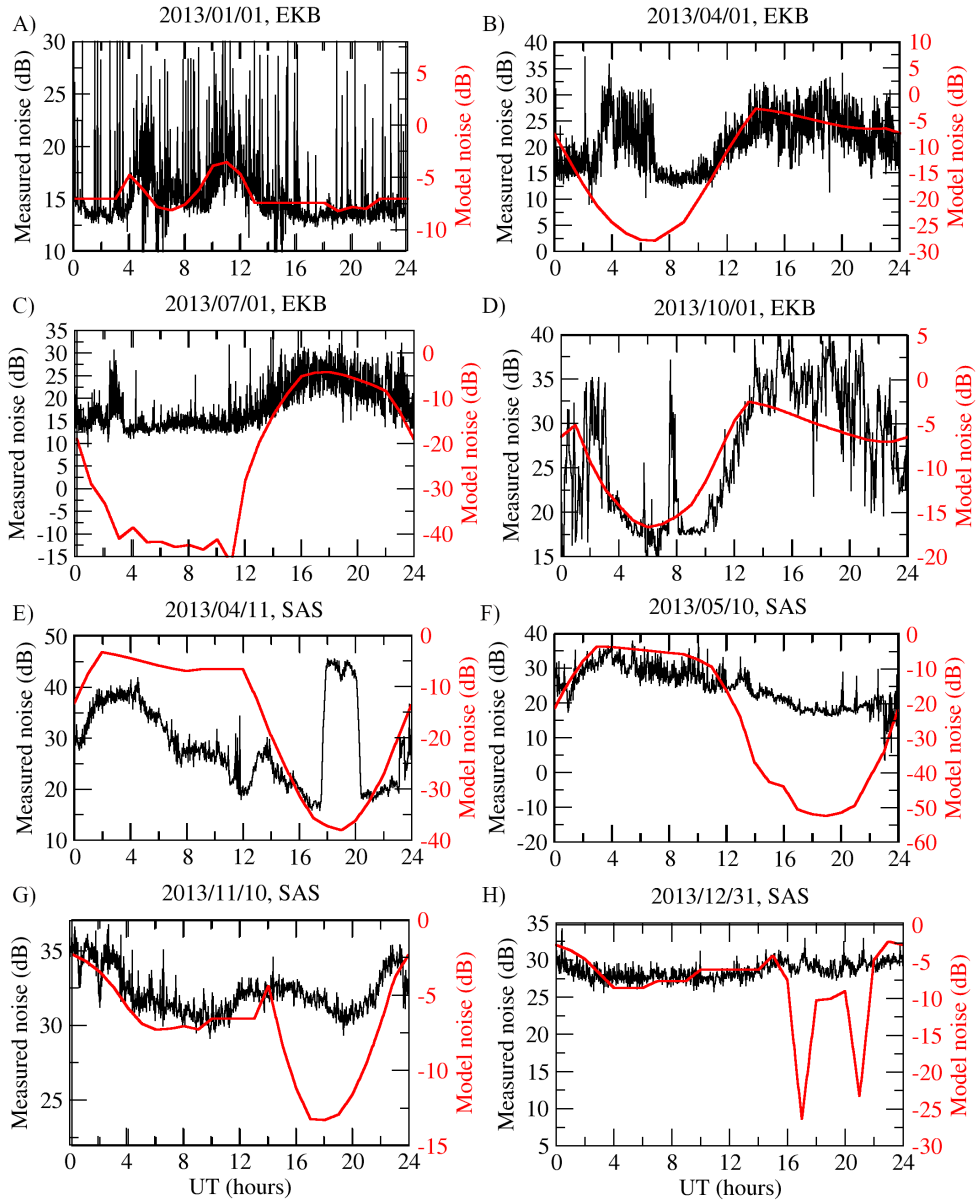
**Figure 5.** Simulated seasonal-diurnal variation of parameters associated with the propagation of radio waves for the EKB radar in 2013 at 10 MHz. We used standard IRI-Ne model for D-layer simulation.

Fig.6 shows some detailed examples of daily variations of the noise on the EKB and SAS radars for different dates and their comparison with our proposed model when we use the Danilov D-layer model for taking into account absorption at lower altitudes, the IRI-2016 ionosphere model for taking into account propagation effects, and NRLMSISE-00 neutral atmosphere model for calculating the electron collision frequency.

As might have been expected from Fig.5, the various panels in Fig.6 show a satisfactory agreement between the observations and the model at high noise levels, but there is generally a strong disagreement when the model noise level is predicted to be low. We see two possibilities that could explain this situation. One is that there may well be a saturation effect associated with analog and digital sensitivity levels of the radars. Alternatively, or even in association with instrumental noise, cosmic noise could be a factor, as it can sometimes be as high as 20 dB below anthropogenic noise, as shown in (ITU-R P.372-14, 2020)(Figs.2,39). Cosmic noise comes from much higher elevation angles and could make a significant contribution when anthropogenic noise is not too strong because of absorption. We have not queried this question any further as the focus of the present paper is anthropogenic sources from the ground. Our model of these contributions produces the bright arc patterns in Fig.4. The important message is that these arcs fit well with the notion of noise from anthropogenic sources.

To demonstrate that saturation effects are very real, we introduce Fig.7. Fig.7A and B show the results of a statistical comparison between the model and the observations using the EKB and KER radar data in the year 2013. The color shows the number of cases when a particular combination of experimental and model noise values was obtained.

Consider Fig. 7A first: clearly, when the observed noise level is less than 20 dB, there is no connection between the predicted noise level and the observed one. However, when the observed noise level is greater than 20 dB there is a linear relation between pre-



**Figure 6.** Comparison of model (red line) and measured daily noise variations (black line) on radars EKB (beam 2, A-D) and SAS (beam 7, E-H), at 10MHz



diction and observations. From this it should be clear that the measured EKB noise levels are saturated below 20 dB, thereby having nothing to do with ionospheric absorption. By contrast, above 20 dB, the effects of ionospheric absorption are seen. The clear implication is that the model cannot be used below 20 dB in the EKB case because of noise saturation effects affecting the observations.

Fig.7B shows that a similar effect takes place for the KER radar. In that case, however, the saturation level is higher (32 or 33 dB), and the physical information that can be extracted from noise variations is for noise levels that are weaker by about 8 to 10 dB.

Fig.7C and D display similar information in a somewhat different way through monthly statistics. For those panels, we kept track of the radar data that could be suitably compared with a numerical interpretation of the observations by the proposed model (as per the numbers inferred from panels A and C, meaning a noise level above 20 dB for the EKB radar and above 32 or 33 dB for the KER radar). This being the case, Fig.7C shows that the probability that the noise level at EKB be 20 dB above the numbers expected from our simulations is always above 60% at all times of the year, with a somewhat higher value (closer to 80%) in June. The numbers are different for KER, as seen from Fig.7D. We note that the statistics are too weak to give any significance to the June peak in that case (a change from 32 dB to 33 dB would put the peak well inside a region of minimum probability).

From our analysis of Fig.7A to D we may conclude that about a half of the daily noise data at EKB is suitable for the numerical interpretation. These periods where the simulations work reasonably well are usually associated with a weak D-layer ionization level. They come mainly from nighttime and autumn-winter months. This much is clear after we take another look at Fig.4. The smaller size of the dataset in KER is caused by its smaller dynamical range (Fig.7B), itself most likely caused by a lower level of distributed surface anthropogenic sources around the radar (Fig.1C), which is isolated in the Southern Indian Ocean.

With the above reservations concerning extra noise sources in mind, the proposed model can be used to build a quiet day curve (the results of which are presented through the red traces in Fig. 6). However, for the model to be put to good use, we need to take into account the saturation effect of the radar sensors at low noise levels. The saturation level clearly differs for each specific radar (Fig.7A,B), and its mechanism and dynamics should be studied in the future. As shown above, this model depends on a number of factors, namely, (1) the trajectory of propagation of the noise signals (or groundscatter signals), (2) the antenna pattern in the elevation plane of propagation, as well as (3) the mode of the received signal as it is affected by propagation in a three-dimensionally inhomogeneous ionosphere. The model used for the ‘quiet’ ionospheric D-layer is also significant in the construction of the quiet day curve. The comparison of observations with model simulations (Fig.4) shows that the use of the traditional IRI-2016 model leads to significant overestimation of the noise level. The Danilov model of the D-layer leads to better fits to observed noise levels than the other models, at least for the EKB radar (Fig.4).

### 3.4 Implications for the modeling of ionospheric absorption

Based on the use of Eqn.(2) for the construction of our model, one can exclude all propagation effects (antenna pattern attenuation  $G_A$ , radio wave attenuation with distance  $A_R$ , and focusing effects  $\overline{I_F}$ ) on the noise level variations  $\overline{I_{N,rcv}}$  as well as exclude attenuation variations in the elevation angles through propagation for a trajectory through an angle  $\alpha$  in the D-layer (valid for a thin non-refracting absorption layer). In other words the intensity is essentially ‘fixed’ through the relation

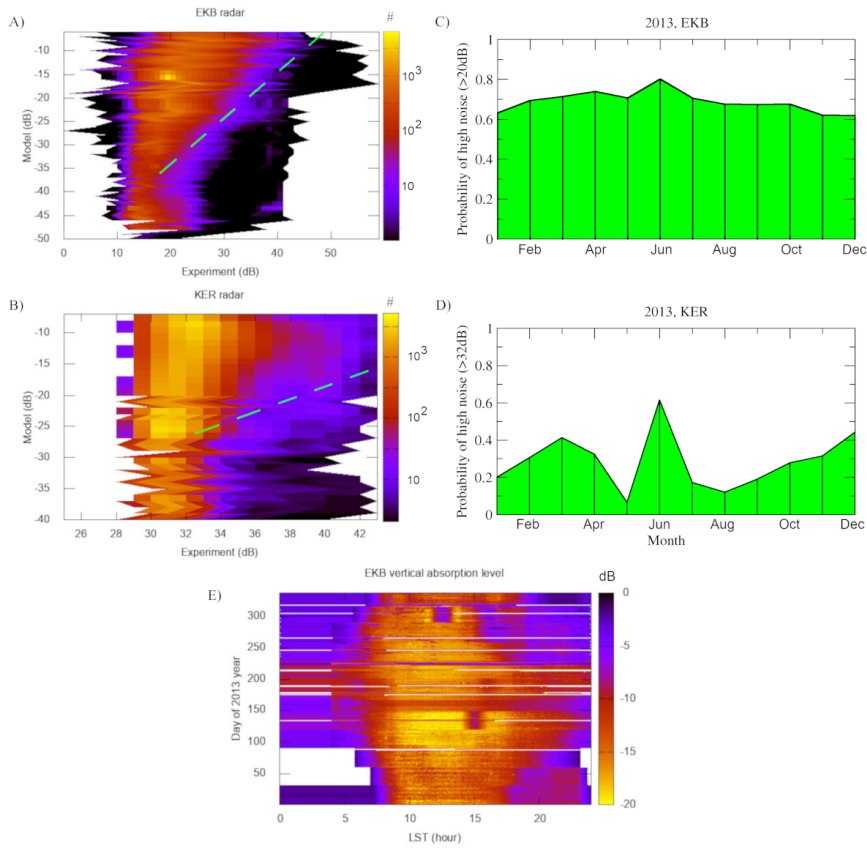


**Figure 7.** Comparison between model and experimental data for the EKB (A) and KER (B) radars and monthly statistics of radar data available for adequate numerical analysis within the framework of the proposed model: for EKB (C) and KER (D) radars. Dashed line in (A,B) corresponds to linear dependence, the color indicates the corresponding number of occurrences of combinations of experiment vs. model values. E) Vertical absorption at 10MHz calculated from experimental EKB noise data using the suggested model.

$$I_{N,fxd}[dB] = 10 \cdot \log_{10} \left( \frac{\overline{I_{N,rcv}}}{I_{0,N} \overline{I_F G_A A_R}} \right) \quad (17)$$

while the vertical absorption becomes

$$A_{t,vert}[dB] = (I_{N,fxd}[dB] - \text{Max}(I_{N,fxd}[dB])) \cdot \sin(\alpha) \quad (18)$$

where the maximum value is calculated over the year to calibrate absorption when it reaches a minimum. As a result, one can obtain an estimate for the equivalent vertical absorption  $A_{t,vert}$  near the radar. Fig.7E shows the seasonal-daily dynamics of the vertical absorption  $A_{t,vert}$  near EKB based on this approach to the analysis of the noise observations at 10 MHz. As one can see, the vertical absorption goes through a maximum at summer daytime. This corresponds well, qualitatively, to the D-layer absorption expected from the IRI-2016 and NRLMSISE-00 models, as shown in Fig.3D.

## 4 Conclusion

In this paper, we have developed a numerical model of the seasonal-diurnal dynamics of the radio noise at polar-oriented HF-radars. The model has focused on four high-frequency mid-latitude coherent scatter radars - EKB from ISTP SB RAS, and SAS, BKS and KER from SuperDARN. The numerical results have been compared with observations.

The results from our simulations give credence to the model proposed earlier in (Berngardt et al., 2018, 2019) for interpreting the radio noise level in terms of the spatial focusing of ground sources of anthropogenic origin in the vicinity of the ‘dead zone’ propagation boundary. Using the IRI-2016 and NRLMSISE-00 models, it has been shown here that seasonal-diurnal variations of the noise level can be explained within the framework of this model through a combination of propagation, absorption and antenna pattern factors.

We have demonstrated that the seasonal-diurnal patterns observed in radio noise (with a maximum in the region of the solar terminator) is associated with variations in the total absorption of the signal over the propagation trajectory to the border of the dead zone. We have also shown that an observed decrease in the noise intensity in the winter noon area in the EKB and SAS radars (not detected with the BKS radar) can be explained by an additional attenuation of the signal by the antenna beam pattern at high elevation angles.

The agreement with observations is particularly good near the terminator where the noise level is greatest. This has allowed to us compare the absorption computed from different D region models and compare the resulting noise levels with observations. We found that the absorption levels, when integrated along the ray paths, were too high when using the standard IRI-2016 D-layer model. However, the agreement with observations based on the use of the FIRI (McKinnell & Friedrich, 2006) and Danilov (Danilov et al., 1995) D-layer models was much better.

The above notwithstanding, in spite of a good qualitative agreement of the seasonal-diurnal model variations with observations, quantitative simulation results demonstrate that the model predicts far less noise than observed away from the terminator during sunlit conditions. There are only two possible explanations: either the model produces too much absorption, or there is another source of noise that does not involve ground-based anthropogenic sources. In the former case, one would have to face the fact that the model produces realistic amounts of absorption at other times, particularly near the terminators. In the latter case there are two possibilities, both of which must be present

but were not considered for our model based on ground sources: cosmic background noise, which comes from above and would favor larger elevation angles, and instrumental noise, i.e., saturated noise counts. The ability to measure absorption variations from radar noise measurements depends on the surrounding anthropogenic noise level - the higher the noise level, the stronger absorption events the radar can study. For radars with low anthropogenic noise level, such as KER, it may be difficult to study strong vertical absorption events from the noise data.

The main message to carry from the present study is that 1) the mechanism proposed in (Berngardt et al., 2018, 2019) does very well near the terminator where the noise level is at its strongest Also, 2) there are additional noise sources to worry about, be they instrumental or of cosmic origin. Finally 3) the present model should provide a useful tool for the assessment of absorption on a day-to-day basis. This means that we could use the present numerical model or its successors to extract important information from the dynamics of noise measured by pole-oriented coherent scatter radars in the 8 to 20 MHz range.

It should be kept in mind that the results presented here can only be considered as preliminary, as they use reference ionospheric model IRI-2016 to calculate the propagation trajectory. For more correct calculations of the propagation path one really ought to take into account actual ionospheric refraction, estimated either from radar data (using, for example, ground-scatter signals in combination with measured elevation angles) or from ionospheric electron density measurements by ionosondes. This approach will be considered in future studies.

### Acknowledgments

The data of EKB radar were obtained using the equipment of Center for Common Use 'Angara' <http://ckp-rf.ru/ckp/3056/> and available at [http://sdrus.iszf.irk.ru/ekb/page\\_example/simple](http://sdrus.iszf.irk.ru/ekb/page_example/simple). The work of EKB radar was financially supported by the Ministry of Science and Higher Education of Russian Federation. Work of OB and AM was supported by joint RFBR-CNRS grant # 21-55-15012 NCNLa. JPSM receives support from the Canadian NSERC. The authors acknowledge the use of SuperDARN data. SuperDARN is a collection of radars funded by national scientific funding agencies of Australia, Canada, China, France, Italy, Japan, Norway, South Africa, United Kingdom and the United States of America. We thank all participants in the worldwide SuperDARN collaboration for the distribution of SuperDARN data via <http://vt.superdarn.org/tiki-index.php?page=Data+Access>. The Saskatoon SuperDARN radar operations are specifically funded by Canadian Space Agency contracts and by a Major Science Initiative from Canada Foundation for Innovation. The SuperDARN Kerguelen radar is operated by IRAP (CNRS, Toulouse University and CNES) and is funded by IPEV and CNRS through INSU and PNST programs. The SuperDARN Blackstone radar is operated by Virginia Tech with funding from the National Science Foundation under award AGS-1935110.

### References

- Arnold, N. F., Cook, P. A., Robinson, T. R., Lester, M., Chapman, P. J., & Mitchell, N. (2003). Comparison of D-region Doppler drift winds measured by the SuperDARN Finland HF radar over an annual cycle using the Kiruna VHF meteor radar. *Annales Geophysicae*, *21*(10), 2073–2082. doi: 10.5194/angeo-21-2073-2003
- Berngardt, O. I. (2020). Noise level forecasts at 8-20 MHz and their use for morphological studies of ionospheric absorption variations at EKB ISTP SB RAS radar. *Advances in Space Research*, *66*(2), 278 - 291. doi: 10.1016/j.asr.2020.04.005
- Berngardt, O. I., Fedorov, R. R., Ponomarenko, P., & Grkovich, K. V. (2020).

- Interferometric calibration and the first elevation observations at EKB  
ISTP SB RAS radar at 10-12 MHz. *Polar Science*, 100628. doi: 10.1016/j.polar.2020.100628
- Bergardt, O. I., Ruohoniemi, J. M., Nishitani, N., Shepherd, S. G., Bristow, W. A., & Miller, E. S. (2018). Attenuation of decameter wavelength sky noise during x-ray solar flares in 2013–2017 based on the observations of midlatitude HF radars. *Journal of Atmospheric and Solar-Terrestrial Physics*, 173, 1–13. doi: 10.1016/j.jastp.2018.03.022
- Bergardt, O. I., Ruohoniemi, J. M., St-Maurice, J.-P., Marchaudon, A., Kosch, M. J., Yukimatu, A. S., . . . Lester, M. (2019). Global Diagnostics of Ionospheric Absorption During X-Ray Solar Flares Based on 8- to 20-MHz Noise Measured by Over-the-Horizon Radars. *Space Weather*, 17(6), 907-924. doi: 10.1029/2018SW002130
- Bilitza, D. (1997). International reference ionosphere - Status 1995/96. *Advances in Space Research*, 20(9), 1751-1754. doi: [https://doi.org/10.1016/S0273-1177\(97\)00584-X](https://doi.org/10.1016/S0273-1177(97)00584-X)
- Bilitza, D., Altadill, D., Truhlik, V., Shubin, V., Galkin, I., Reinisch, B., & Huang, X. (2017). International Reference Ionosphere 2016: From ionospheric climate to real-time weather predictions. *Space Weather*, 15(2), 418-429. doi: 10.1002/2016SW001593
- Bilitza, D., & Reinisch, B. (2008). International Reference Ionosphere 2007: Improvements and new parameters. *Advances in Space Research*, 42(4), 599-609. doi: 10.1016/j.asr.2007.07.048
- Bland, E. C., Heino, E., Kosch, M. J., & Partamies, N. (2018). SuperDARN radar-derived HF radio attenuation during the September 2017 solar proton events. *Space Weather*. doi: 10.1029/2018sw001916
- Bland, E. C., Partamies, N., Heino, E., Yukimatu, A. S., & Miyaoka, H. (2019). Energetic Electron Precipitation Occurrence Rates Determined Using the Syowa East SuperDARN Radar. *Journal of Geophysical Research: Space Physics*, 124(7), 6253–6265. doi: 10.1029/2018JA026437
- Danilov, A., Rodevich, A., & Smirnova, N. (1995). Problems with incorporating a new D-region model into the IRI. *Advances in Space Research*, 15(2), 165-168. (Off Median Phenomena and International Reference Ionosphere) doi: 10.1016/S0273-1177(99)80042-8
- Danilov, A., Smirnova, N., Blix, T., & Thrane, E. (2002). A new concept of the D-region modeling at high latitudes. *Advances in Space Research*, 29(6), 919-927. doi: 10.1016/S0273-1177(02)00048-0
- Gomonov, A. D., Yurik, R. Y., Shapovalova, Y. A., Cherniakov, S. M., & Kalitenkov, N. V. (2019, jul). The Analysis of Electron Density Values According to Simulations by IRI Model and from Experimental Measurements by Partial Reflection Radar. In *2019 Russian Open Conference on Radio Wave Propagation (RWP)*. IEEE. doi: 10.1109/rwp.2019.8810341
- ITU-R P.372-14. (2020, 09). *Recommendation ITU-R P.372-14 (08/2019). Radio noise*. Retrieved from <https://www.itu.int/rec/R-REC-P.372-14-201908-I/en>
- Kravtsov, Y. (1968). On two new asymptotic methods in the theory of wave propagation in inhomogeneous media. Overview (in russian). *Acoustical journal*, 14(1), 1-24.
- Kravtsov, Y., & Orlov, Y. (1983). Caustics, catastrophes, and wave fields. *Soviet Physics Uspekhi*, 26(12), 1038.
- McKinnell, L., & Friedrich, M. (2006). Results from a new auroral lower ionosphere model. *Advances in Space Research*, 37(5), 1045-1050. (Advances in Specifying Plasma Temperatures and Ion Composition in the Ionosphere) doi: 10.1016/j.asr.2004.11.008
- Pederick, L. H., & Cervera, M. A. (2014). Semiempirical Model for Ionospheric

- Absorption based on the NRLMSISE-00 atmospheric model. *Radio Science*, 49(2), 81-93. doi: 10.1002/2013RS005274
- Ponomarenko, P., Iserhienhien, B., & St.-Maurice, J.-P. (2016). Morphology and possible origins of near-range oblique HF backscatter at high and midlatitudes. *Radio Science*, 51(6), 718-730. doi: 10.1002/2016rs006088
- Samson, J. C., Greenwald, R. A., Ruohoniemi, J. M., Frey, A., & Baker, K. B. (1990). Goose Bay radar observations of Earth-reflected, atmospheric gravity waves in the high-latitude ionosphere. *Journal of Geophysical Research: Space Physics*, 95(A6), 7693-7709. doi: 10.1029/JA095iA06p07693
- Schunk, R. W., & Nagy, A. F. (2000). *Ionospheres: Physics, Plasma Physics, and Chemistry*. Cambridge University Press. doi: 10.1017/CBO9780511551772
- Shepherd, S. G. (2014). Altitude-adjusted corrected geomagnetic coordinates: Definition and functional approximations. *Journal of Geophysical Research: Space Physics*, 119(9), 7501-7521. doi: <https://doi.org/10.1002/2014JA020264>
- Shepherd, S. G. (2017). Elevation angle determination for SuperDARN HF radar layouts. *Radio Science*, 52(8), 938-950. doi: 10.1002/2017RS006348
- Sterne, K. T., Greenwald, R. A., Baker, J. B. H., & Ruohoniemi, J. M. (2011). Modeling of a twin terminated folded dipole antenna for the Super Dual Auroral Radar Network (SuperDARN). In *2011 IEEE RadarCon (RADAR)* (p. 934-938). doi: 10.1109/RADAR.2011.5960673
- Tinin, M. V., Afanasyev, N. T., Mikheev, S. M., Pobedina, A. P., & Fridman, O. V. (1992). On some problems of the theory of radio wave propagation in a randomly inhomogeneous ionosphere. *Radio Science*, 27(2), 245-255. doi: 10.1029/91RS02921
- Zawdie, K. A., Drob, D. P., Siskind, D. E., & Coker, C. (2017). Calculating the absorption of HF radio waves in the ionosphere. *Radio Science*, 52(6), 767-783. doi: 10.1002/2017RS006256